

Journal of Biomedical Optics

BiomedicalOptics.SPIEDigitalLibrary.org

Surface plasmon resonance–based infrared biosensor for cell studies with simultaneous control

Alexander Zilbershtein
Amir Bein
Vladislav Lirtsman
Betty Schwartz
Michael Golosovsky
Dan Davidov

Surface plasmon resonance–based infrared biosensor for cell studies with simultaneous control

Alexander Zilbershtein,^{a,*†} Amir Bein,^{b,†} Vladislav Lirtsman,^a Betty Schwartz,^b Michael Golosovsky,^a and Dan Davidov^a

^aHebrew University of Jerusalem, The Racah Institute of Physics, 91904 Jerusalem, Israel

^bHebrew University of Jerusalem, School of Nutritional Sciences, Institute of Biochemistry, Food Science and Nutrition, The Robert H. Smith Faculty of Agriculture, Food and Environment, P.O. Box 12, 76100 Rehovot, Israel

Abstract. We report a label-free infrared surface plasmon biosensor with a double-chamber flow cell for continuous monitoring of morphological changes in cell culture exposed to various stimuli. In this technique, the monolayer of cultured cells is divided into two halves by a barrier, allowing the treatment of one half while the other serves as control. We demonstrate the advantages of this setup in test experiments that track kinetics of the IEC-18 cell layer response to variations in extracellular Ca^{2+} concentration. The sensitivity of the presented method was found to be an order of magnitude higher compared to the single-chamber biosensor. © 2014 Society of Photo-Optical Instrumentation Engineers (SPIE) [DOI: [10.1117/1.JBO.19.11.111608](https://doi.org/10.1117/1.JBO.19.11.111608)]

Keywords: sensors; surface plasmons; waveguides; cells; infrared spectroscopy; Fourier transform spectroscopy.

Paper 140060SSR received Jan. 31, 2014; revised manuscript received May 13, 2014; accepted for publication May 27, 2014; published online Jun. 27, 2014.

1 Introduction

The ability to examine living cells in their natural environment and under physiological conditions is crucial for both basic and applied biological research. The conventional approach for working with cells in a biological laboratory implies target-based labeling. The majority of the cell-based assays measure a specific cellular event by tagging a particular target with a fluorescent label.¹ Although this approach yields very specific and precise information, it is invasive and involves robust, time-consuming, and expensive procedures. Therefore, a biosensor that can provide a label-free, noninvasive, and real-time record of cellular activity and health would be desired.

The label-free biosensors include microbalance, impedance, and optical sensors.² The latter has widespread utilization in biological research and today they present a well-established analytical tool for probing biomolecular interactions.^{3,4} Among the most important optical biosensors are surface plasmon resonance (SPR) and resonant waveguide grating (RWG) sensors. These sensors operate in the visible wavelength range and are mostly used for biomolecule affinity characterization and determination of molecular binding kinetics.^{5,6} Successful implementation of optical biosensing techniques in biochemical assays encouraged the development of similar techniques at the cellular level.^{7,8} Also, living cells activities, such as cell–substrate adhesion and spreading,^{9,10} proliferation,^{8,11,12} and toxicity^{13,14} were examined by SPR or RWG biosensors operating in the visible range. These sensors have a short penetration depth ($\sim 0.1 \mu\text{m}$) and they measure a thin cell layer close to the substrate. This is especially beneficial for probing cell–substrate adhesion or protein trafficking across the cell basal membrane. The probing of cellular events occurring further away from the

substrate (cell height, cell–cell adhesion) requires sensors with a longer penetration depth. This can be done with the infrared evanescent wave sensors that have a long penetration depth which is comparable to cell height.^{8,14}

The label-free biosensors shall have the ability of multichannel measurements including control channels.³ Indeed, in contrast to labeling approaches that are capable of revealing very specific binding interactions, the label-free optical biosensors for cell assays are integrative since they measure the stimulus-induced change of some global physical parameters of the cells, such as refractive index. Yet, since cell activities and cell cycles might vary among various cell samples, the differences in their cellular status can affect the stimulus-induced changes. This requires special control of the cellular status which is best achieved by multichannel measurements.^{3,15} Although multichannel functionality is easily implemented in the design of optical biosensors operating in the visible range, its incorporation into an infrared biosensor is not straightforward due to the huge difference in the components, sources, and detection schemes.

We report here an SP-based infrared biosensor for cell studies where we have implemented the multichannel functionality. Our sensor incorporates one homogeneous cell sample grown on the same substrate and divided into two separate chambers only at the measurement stage (this is in contrast to Ref. 14 that used two samples of the same cell culture grown on two different substrates). We optically monitor both chambers while applying the stimulus to only one of them. This strategy allows distinguishing between the stimulus-induced effect and other biological, naturally occurring changes that are normal features of cell cultures that originate from the cell cycle, proliferation, and differentiation.

Our sensor is based on the infrared SP wave which is the electromagnetic wave propagating at the metal/cells' interface.

*Address all correspondence to: Alexander Zilbershtein, E-mail: zibzilber@gmail.com

†These authors contributed equally to this work.

It probes the refractive index of the cells. The latter is sensitive to the cell–cell and cell–substrate attachment, as well as to cell morphology and integrity of the cell monolayer. In the case of the intact cell monolayer, additional guided transverse magnetic (TM) mode resonances usually appear. These waveguide modes travel inside the cell monolayer and they yield complementary information about the average cell layer height and layer integrity.^{8,10,12}

To demonstrate operation of the double-chamber SP-based infrared biosensor, we utilized an *in vitro* cell culture model of IEC-18 and IEC-6 intestinal epithelial cells. To test the advantages of this technique in the dual channel regime, we measured the response of a confluent IEC-18 cell monolayer to morphological perturbations induced by a well-known stimulus—alterations in extracellular Ca^{2+} concentration.^{16–18} We demonstrate that the dual channel protocol is capable of detecting very small effects resulting from Ca^{2+} depletion and replenishment, while the single channel protocol does not provide unambiguous information on the changes at this scale.

2 Cell Probing by Infrared SP Spectroscopy

2.1 Principles of SP-Based Spectroscopy

The SP is the surface electromagnetic wave that travels along a metal–dielectric (gold and cells in our case) interface and decays exponentially in the direction perpendicular to the interface.¹⁹ It is usually excited in the attenuated total reflection regime using

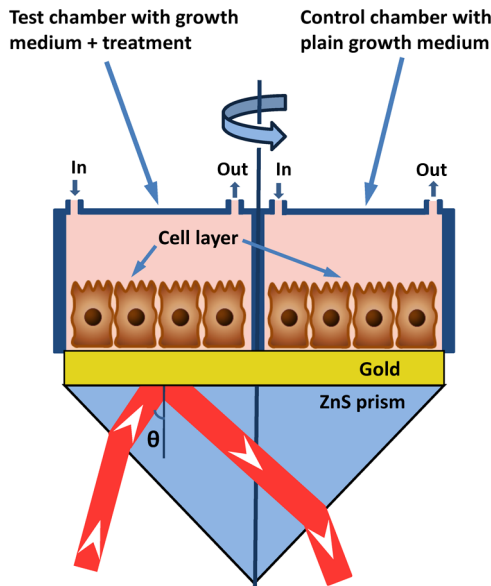


Fig. 1 A double-chamber flow cell for Fourier Transform Infrared–Surface Plasmon Resonance (FTIR–SPR) measurements of living cells. The cell sample is grown homogeneously on the prism surface and is divided into two halves with a separating barrier only at the measuring stage. One chamber undergoes treatment with some stimulus while another chamber serves as control. The infrared beam is reflected from one half of the prism base and its intensity is measured. This yields information on the refractive index of the cell layer in the corresponding chamber. After each measurement, the prism is rotated 180 deg around the vertical axis, and reflectivity from the other chambers is measured (control). Then the prism is rotated -180 deg backward to the initial position and the measurement is repeated. The minimal temporal resolution of our measurements is ~ 1.5 min (40 s for one-channel measurement and 20 s for switching between the channels).

a prism coupler (Fig. 1). The SP wavevector k_{sp} is determined by the complex dielectric permittivity of gold, ϵ_{Au} , and cells, $\epsilon_{\text{cell}} = (n_{\text{cell}} + i\kappa_{\text{cell}})^2$. The propagation component of the SP wavevector is given by $k(x)_{\text{sp}} = k_0(\epsilon_{\text{Au}}\epsilon_{\text{cell}}/\epsilon_{\text{Au}} + \epsilon_{\text{cell}})^{1/2}$. The SP is excited at a certain angle/wavelength at which the real part of its wavevector matches the x -component of the incident light wavevector, k_0 : $k'(x)_{\text{sp}} = n_{\text{prism}}k_0 \sin \theta$. Here, n_{prism} is the prism refractive index and θ is the angle of incidence (Fig. 1). The resonant condition is given by

$$n_{\text{prism}} \sin \theta = \text{Re} \left[\left(\frac{\epsilon_{\text{Au}}\epsilon_{\text{cell}}}{\epsilon_{\text{Au}} + \epsilon_{\text{cell}}} \right)^{1/2} \right]. \quad (1)$$

Since ϵ_{cell} and ϵ_{Au} are wavelength-dependent, the resonant condition singles out a certain wavelength at which the reflectivity achieves the minimum (Fig. 2). The dielectric permittivity of the cells ϵ_{cell} at the wavelength corresponding to the SPR minimum can be calculated from the dielectric permittivity of the gold ϵ_{Au} , refractive index of the prism n_{prism} , and the angle of incidence θ . This fact is the basis underlying the SPR spectroscopy—by measuring the SPR minima wavelength one finds n_{cell} , the refractive index of the cells adjacent to the gold.^{8,20}

2.2 Studying Living Cells with an Infrared SP Wave

In the context of living cell probing by the SP wave, there are two important length scales: the SP lateral propagation length and the SP penetration depth. In the infrared range ($\lambda = 0.75$ to $2.7 \mu\text{m}$ in our case), the SP propagation length is $L_x = 50$ to $150 \mu\text{m}$ (Refs. 8 and 12) and it is bigger than the lateral typical cell size of $20 \mu\text{m}$. Hence, in the confluent cell monolayer, the SP wave travels across a few cells and probes the effective refractive index of the cell layer which is an average over several cells. When the cell layer is not fully confluent, the layer probed by the SP wave consists of regions with different refractive

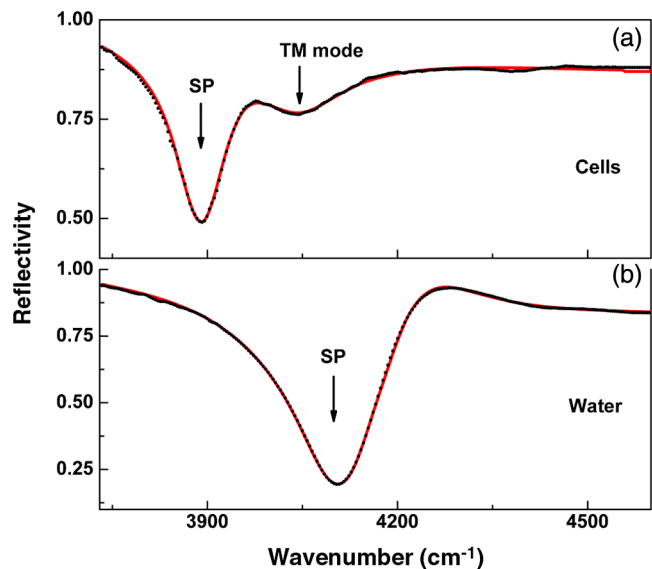


Fig. 2 Measured infrared reflectivity spectra (black dots) and fitting using Fresnel formulae for reflectivity from a multilayer (red solid line): (a) ZnS prism/gold/cells, (b) ZnS prism/gold/water. The nominal gold film thickness is 18 nm and the angle of incidence is 35 deg. The surface plasmon (SP) and TM-waveguide mode resonances are shown by arrows.

indices (cells and growth medium). If the size of these regions is less than the SP propagation length, a single SPR corresponding to the mean refractive index of the mixture appears.⁸ In the opposite case, two separate SPRs appear, corresponding to refractive indices of media and cells.

Another important length scale is the SP penetration depth δ_z , namely the decay length of the SP electric field in the direction normal to the interface.⁸ Due to its evanescent nature, the SP wave probes the effective refractive index of the cells which is a weighted average in the direction normal to the interface

$$\begin{aligned} \sqrt{\varepsilon_{\text{cell,eff}}} &= (n_{\text{cell}} + ik_{\text{cell}})_{\text{eff}} \\ &= \frac{1}{\delta_z} \int_0^{\infty} [n(z) + ik(z)] \exp(-z/\delta_z) dz. \end{aligned} \quad (2)$$

The SP penetration depth is growing with a wavelength^{8,12} reaching $\delta_z = 3 \mu\text{m}$ in the infrared range, at $\lambda = 2.6 \mu\text{m}$. Working in the infrared range is beneficial for living cells studies. Indeed, with such a long penetration depth, the SP probes most of the cell volume. This is in contrast to the visible range where the typical SP penetration depth is much smaller, $\delta_z \sim 0.1 \mu\text{m}$. The infrared SP wave yields information about (a) the basal part of the cells, which represents the quality of the cell–substrate attachment and (b) the apical part of the cells—complete information about the quality of the cell–cell attachment, including all kinds of junctions: adherence (responsible for cell–cell adhesion) and tight junctions (responsible for paracellular permeability).

Cells are nonhomogeneous objects that consist of water and organic content. The real part of the cell refractive index can be written as

$$n_{\text{cell}} = f \cdot n_{\text{organic}} + (1 - f)n_{\text{water}}, \quad (3)$$

where n_{water} is the refractive index of the water, and f and n_{organic} are the fraction of organic content of the cell and its average refractive index, correspondingly. The real part of the cell refractive index exceeds that of the water since the refractive index of organic substances is higher than that of water.^{21,22} However, since the cells consist of $\sim 70\%$ water, this difference is only $n_{\text{cell}} - n_{\text{water}} \sim 0.03 - 0.04$ (Figs. 3 and 4) and it depends on wavelength, cell line, and cell polarization.²³ Hence, the real part of the cell's effective refractive index measures the amount of the cell biomass in close proximity to the interface. The imaginary part of the cell's effective refractive index is determined by the absorption and scattering of the SP wave and provides information about the cell morphology.^{10,23} Various cell features, such as cell adhesion to substrate, cell spreading and polarization, and opening and closure of tight junctions, are associated with the cell morphological changes, which lead to dynamic biomass redistribution of the cell content.²⁴ Our FTIR-SPR biosensor senses the changes of the cell's effective refractive index induced by these biomass redistribution processes^{8,10,25} and can effectively pinpoint the kinetics of the corresponding cellular processes.

2.3 Studying Cell Monolayer with Waveguide Resonances

An epithelial cell monolayer cultured on a metal-coated dielectric prism and immersed into buffer medium represents a dielectric multilayer with progressively decreasing refractive indices.

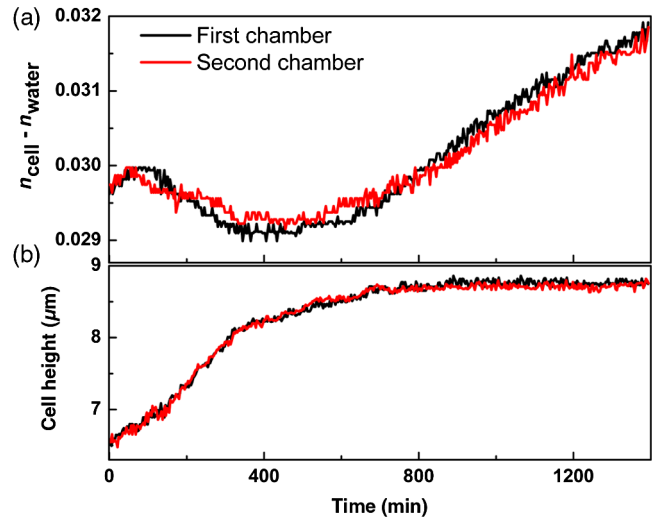


Fig. 3 Dynamics of the real part of the IEC-6 cell refractive index n_{cell} (a) and average cell height (b) measured by double-chamber infrared SP biosensor. The temporal resolution of these measurements is 3 min. Cells (1×10^6) were seeded on the ZnS prism and cultured for 48 h. Both chambers were filled with growth medium (red line—first chamber and black line—second chamber). The difference between the refractive indices of the cells and water at SPR wavelength ($2.55 \mu\text{m}$) is presented. The variation in n_{cell} and cell height during the course of experiment is associated with the cell adaptation, polarization, proliferation, and growth. The cell refractive index difference between two chambers does not exceed 3×10^{-4} RIU during the whole experiment, while the average cell height difference between the chambers does not exceed $0.1 \mu\text{m}$.

Such multilayer supports propagation of leaky waves (waveguide modes). The waveguide mode propagates inside the cell layer and its resonant wavelength sensitively depends on the cell layer height. Indeed, the waveguide resonance occurs when the total phase shift for round-trip propagation through the dielectric multilayer is

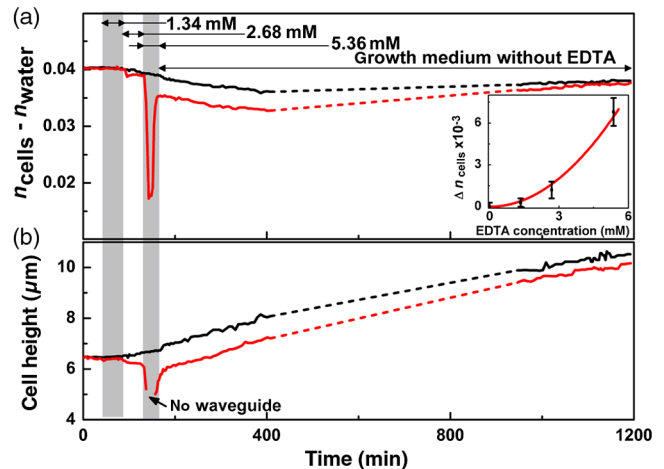


Fig. 4 Short-term dynamics of IEC-18 cells refractive index n_{cell} (a) and average cell height (b) in response to different concentrations of extracellular Ca^{2+} . The latter was induced by the addition of three different sequentially administered concentrations of ethylenediaminetetraacetic acid (EDTA). Red line corresponds to the chamber with low Ca^{2+} (treatment) and black line corresponds to the chamber with normal concentration of Ca^{2+} (control). Duration of every EDTA treatment is 40 min. The temporal resolution of these measurements is 3 min. Inset: The difference between cell refractive index in the treatment chamber and that in the control chamber, Δn_{cell} , versus EDTA concentration in growth medium, C_{EDTA} (black squares). Red line represents the quadratic dependence $\Delta n_{\text{cell}} \sim C_{\text{EDTA}}^2$.

a multiple of 2π . For p -polarized incident light, these relations yield a set of resonant wavelengths corresponding to TM_1 , TM_2, \dots modes,

$$\lambda_{TM} = \frac{4\pi n_{\text{cell}} h \cos \theta}{2\pi m - \phi_{\text{cg}} - \phi_{\text{cm}}}, \quad (4)$$

where h is the average height of the cell layer, θ is the incident angle, ϕ_{cg} and ϕ_{cm} are the phase shifts on reflection from the cell–gold and cell–medium interfaces, respectively, and $m = 1, 2, \dots$. The waveguide mode resonances enable direct monitoring of the average cell height and the integrity of a cell monolayer.^{12,25} Waveguide modes, which appear as short-wave satellites of the SPR, can be detected by the same optical setup used for SP spectroscopy.

Together, the SPR, which probes the average refractive index of the cells, and the waveguide mode resonance, which probes the cell height and cell–cell attachment, make the basis of a very informative label-free sensor of cell activity.

3 Materials and Methods

3.1 FTIR-SPR Experimental Setup and Measurement Protocol

The infrared multiwavelength beam is emitted from the external port of the FTIR spectrometer (Bruker Equinox 55).^{8,12} The collimated beam passes through a polarizer mounted on the computer-controlled motorized rotating stage. The polarized beam is reflected from the Au-coated right-angle ZnS prism ($20 \times 40 \text{ mm}^2$ base, ISP Optics, Inc., Irvington, New York), on which a monolayer of cells is grown above the gold layer. The infrared beam is then focused onto a liquid-nitrogen-cooled MCT detector. The p -polarized beam serves for SP excitation, while the s -polarized beam is used as a background. Each single measurement consists of recording the p - and s -reflectivity spectra (that takes approximately 40 s) and represents an average of eight scans with a 4 cm^{-1} resolution.

The biosensor chip for living cell measurements is shown in Fig. 1. The ZnS prism with an 18-nm thick Au coating is attached hermetically to the double-chamber flow cell which is then mounted on the computer-controlled motorized rotating stage. Each chamber has a volume of about $\sim 1 \text{ ml}$ and is $\sim 5 \text{ mm}$ thick. The flow cell is equipped with a cooler/heater system operated by a temperature controller that maintains the same temperature in both chambers. The medium flow is controlled independently in each chamber by the double-syringe pump (NE-4000, New Era Pump Systems, Inc., Farmingdale, New York). The cells are cultured homogeneously on the prism base and form a tight monolayer. This monolayer is divided into two parts by the barrier of the double-chamber flow cell. This is done only at the measuring stage, 48 h after cell seeding.

The infrared reflectivity spectra were measured sequentially from the test and control chambers. The collimated and polarized infrared beams are incident upon one half of the prism base (Fig. 1) in order to measure the reflectivity from one chamber. After every measurement, the prism with the flow cell is rotated 180 deg around the vertical axis in such a way that the infrared beam is now incident upon the other prism half. The measurement from the sample in the second chamber is taken (control measurement) and then the prism is rotated -180 deg backward to the initial position. Comparison between measurements from the two chambers yields direct

information about stimulus-induced changes in the cells without undesired background resulting from the sample's cellular status.

3.2 Analysis of the SPR Spectra

To analyze the SPR spectra, we used a fitting procedure based on the Fresnel optical model for reflectivity from a multilayer.²³ The simulation algorithm consists of two parts. The first part involves two calibration measurements with two known analytes: pure water (optical constants taken from Ref. 26) and air ($n_a = 1$, $\kappa_a = 0$). The measured spectrum (black circles) and the simulated curve (red solid line) for a prism/gold/water trilayer are shown in Fig. 2(b). This part yields the optical constants of the Au film (which can differ from those of bulk gold²⁷), beam divergence, and exact values of incident angle and thickness of the Au film. The optical constants of gold were simulated using the Lorentz–Drude model, while the starting parameters for the fitting procedure were taken from Ref. 28. The second part of the analysis uses the Fresnel equations and parameters from the first part to find the optical constants (n_d , κ_d) of the cells. The measured reflectivity spectrum (black circles) and the simulated curve (red solid line) for the prism/gold/cells trilayer are shown in Fig. 2(a).

3.3 Cell Culture, Measurements and Ca^{2+} Treatment

3.3.1 Cell culture

Rat intestinal epithelial cells (IEC-6) were routinely cultured in growth medium containing Dulbecco's modified Eagle medium (DMEM) (Sigma-Aldrich, Inc., St. Louis, Missouri), supplemented with 10% (v/v) fetal bovine serum (FBS) (SAFC Biosciences, Lenexa, Kansas) and penicillin streptomycin nystatin—solution (Biolab-chemicals, Jerusalem, Israel) 0.2% (v/v). Rat intestinal epithelial cells (IEC-18) were cultured in growth medium containing DMEM, supplemented with 10% (v/v) FBS, 1% (v/v) Glutamine (Biological Industries, Beit Haemek, Israel), and 1% (v/v) Penstrep (Biological Industries, Beit Haemek, Israel). Cells were cultured in a 37°C humidified atmosphere of 95% air and 5% CO_2 . When cells reached 100% confluence, the growth medium was removed, cells were washed with PBS, and 2.0 ml of trypsin-ethylenediaminetetraacetic acid (EDTA) solution (Biological Industries, Beit Haemek, Israel) were added. After the cells were dispersed, 4.0 ml of growth medium was added, and the cells were centrifuged. Cells were resuspended in 1 ml of fresh growth medium and counted with a Hemocytometer (Hausser Scientific, Horsham, Pennsylvania). Cells were seeded on top of the Au-coated ZnS prism which was placed in a holder in order to keep the base side of the prism horizontal. Cells were then cultured in a 37°C humidified atmosphere of 95% air and 5% CO_2 .

In order to speed up tight junction formation, we used a high number of cells (from 1×10^6 to 2×10^6) for seeding on the prism. This number exceeds by a factor of two to four (on the base of cell to area ratio) the number of cells normally seeded when using standard plastic ware. We found that tight junctions are already orderly developed after 48 h of growth.

3.3.2 Measurement protocol

It is important to note that we seeded the cells on the whole prism in one shot in such a way that at the moment of seeding there is only one big chamber. After 48 h, when the cells have been grown, the cell monolayer on the prism was attached to the flow cell under completely sterile conditions. The flow cell contains a separating wall in such a way that the prism surface is divided into two chambers and this occurs only after the cell monolayer has grown.

Each chamber of the flow cell was filled with ~ 1 ml of the same growth medium. The flow cell was then mounted on the rotating stage and connected to the double-channel fluidic system that kept a continuous flow of fresh growth medium at a rate of $6 \mu\text{l}/\text{min}$ in each chamber. The temperature controller kept the entire flow cell at a stable temperature of $37^\circ\text{C} \pm 0.5$ throughout the experiment.

3.3.3 Ca^{2+} depletion experiments

After a short adaptation period, the growth medium was removed from both chambers. The control chamber was refilled with the same growth medium while the test chamber was filled with the growth medium containing some specified concentration of EDTA (this kind of replacement was carried out up to three times with increasing concentrations of EDTA). In order to check the monolayer's restoration capabilities by Ca^{2+} replenishment, the growth medium in both chambers was replaced with fresh growth medium after a predetermined time (40 min in short-term dynamics; 500 and 300 min in long-term dynamics experiments).

4 Results and Discussion

4.1 Test Measurements

To test the operation of our biosensor, we conducted a trial experiment with confluent IEC-6 cells when both chambers were filled with plain growth medium under constant flow and no stimulus was applied. The purpose of this experiment was to check to what extent the cell monolayer behavior was identical in both chambers during a 24-h long measurement. The temporal resolution of these measurements was 3 min.

Figure 3 shows that at the beginning of the measurement, the refractive index of the cells in both chambers is the same, indicating that the cells grew homogeneously on the entire surface of the prism. In the course of time, the refractive index of the cells slowly changes, first due to adaptation following the buffer replacement ($t = 0$ to 400 min), and then due to progressive cell polarization, growth, and proliferation (after $t = 400$ min). The dynamics of cell height as measured by the wavelength of the TM waveguide resonance [Fig. 3(b)] corroborates this explanation. During the first 400 min, the cell height increases from 6.5 to $9 \mu\text{m}$, indicating recovery after the minor shock associated with the buffer replacement. Afterwards, the cell height continues to grow, but more slowly, indicating progressive cell polarization. Notably, Fig. 3 shows that the cell height and the cell refractive index are the same in both chambers during the whole course of measurement. Such experiments were carried out with different cell lines: IEC-6 (Fig. 3) and Caco-2 (data not shown) and different culturing times of the cells on the prism (24 to 72 h). In all these experiments, we obtained consistent results.

Although the overall refractive index variation through the 24 h of measurements is $\sim 3 \times 10^{-3}$ refractive index unit (RIU), the difference between the two chambers does not exceed $\sim 3 \times 10^{-4}$ RIU. This means a 10-fold increase in sensitivity with respect to the single-chamber measurement. Note that the measurement uncertainty associated with the physical sources (temperature instability and its effect on the refractive index, angular misalignment arising from rotation of the prism, polarization instability of the infrared source and discrete noise associated with the spectral resolution of the apparatus) is much smaller, $\sim 10^{-5}$ RIU. Hence, the dominant source of the measurement variability in such an experiment is biological and not instrumental. With respect to cell height, the overall increase during 24 h is $\sim 3 \mu\text{m}$, while the difference between the two chambers is $< 0.1 \mu\text{m}$.

4.2 Ca^{2+} Depletion Experiments

To demonstrate the advantages of the double-chamber protocol over the single-chamber one, we utilized a well-documented cell phenomenon which has been intensively studied by conventional fluorescent labeling, and we measured its kinetics in real time using a label-free SP technique. In particular, we analyzed the response of a fully confluent IEC-18 cell monolayer to different concentrations of extracellular Ca^{2+} in the bathing medium. The latter was altered by the addition of different concentrations of the EDTA chelating agent into the growth medium which contained normal Ca^{2+} levels (1.8 mM). Extracellular Ca^{2+} plays a crucial role in triggering, assembly, and sealing of adherence^{29,30} and tight junctions^{31–33} that are located at the apical part of the cell membrane. The structural integrity and functional polarity of epithelial cells require both cell–substrate and cell–cell adhesions, which give rise to physical and signaling stimuli for the initiation of cell polarization.³⁴ E-cadherin, which is a Ca^{2+} -dependent protein, is an important component of adherence junctions in epithelial cells. Deletion of E-cadherin by siRNA methodology leads to inhibition of cell polarity establishment.³⁵ Tight junctions are protein complexes located at the cell–cell interface and are more apical than adherence junctions. They are responsible for maintaining the epithelial layer impermeable (or selectively permeable). In addition, they also play an important role in the development of epithelial cell polarity.^{33,36} Previously, it was reported that cells which were exposed to low-calcium growth medium did not develop tight junctions, yet, when Ca^{2+} was added, tight junctions evolved, and cell polarization developed.^{17,18} Our aim in this experiment was to track the kinetics of the morphological changes in a cell monolayer under controlled variations in the Ca^{2+} level in growth medium and to compare them with the morphological changes of identical cells under normal Ca^{2+} concentration.

In order to investigate morphological changes of a confluent cell monolayer induced by different extracellular Ca^{2+} concentrations, we conducted two kinds of experiments. In the first one, we studied a short-time exposure of the cell monolayer to the growth medium supplemented with different EDTA concentrations (40 min for each concentration) (Fig. 4). The first two replacements of the treatment medium (1.34 and 2.68 mM of EDTA) reduced the concentration of extracellular Ca^{2+} but did not deplete the growth medium completely from Ca^{2+} . In contrast, the third replacement (5.36 mM of EDTA) caused a total depletion of Ca^{2+} in the medium. Figure 4 shows that the first medium replacement (1.34 mM EDTA) hardly affected

the refractive index of the cells, which means that the adherence and tight junctions did not disassemble and the cells did not undergo significant morphological changes. At the second stage (2.68 mM of EDTA), the refractive index of the cells decreased slightly. We associate this decrease with the beginning of junctions opening and the decreasing height of the circumferential ring of actin filaments.^{16,37} The third step (5.36 mM of EDTA) induced a fast (few minutes) breakdown of adherence and tight junctions, resulting in rapid changes in cell morphology. This process was so fast that it produced wounds in the cell monolayer²⁵ which drastically decreased cell coverage of the gold. This resulted in the sharp drop of the refractive index of the cells at the beginning of this stage. Continuation of junctions opening produced cell relaxation and spreading on the gold surface. This resulted in the increase of the cell coverage of gold and a consequent increase of the effective cell refractive index. At the end of this stage, the growth medium was replaced with fresh normal growth medium (normal Ca^{2+} concentration—1.8 mM) in order to track the buildup of cellular junctions and cell polarization development. As shown in Fig. 4, the full recovery of the cell layer takes ~ 1000 min.

The inset to Fig. 4 shows that the magnitude of the transient change of the cell refractive index correlates nonlinearly to the EDTA concentration, $\Delta n_{\text{cell}} \sim C_{\text{EDTA}}^2$. The nonlinearity implies the threshold-like response of the cells to Ca^{2+} depletion: the cell layer can withstand and counterbalance small levels of Ca^{2+} depletion, but cannot withstand large levels of Ca^{2+} depletion.

The average cell height [Fig. 4(b)] shows that before treatment the cell height in both chambers was the same— $6.5 \mu\text{m}$. This is lower than the normal cell height; hence, the cells are not fully polarized. Indeed, the cell height in the control chamber slowly grows with time to $10 \mu\text{m}$, indicating progressive cell polarization. The EDTA treatment of the measurement chamber reduces the cell height (the cell monolayer is less rigid since the

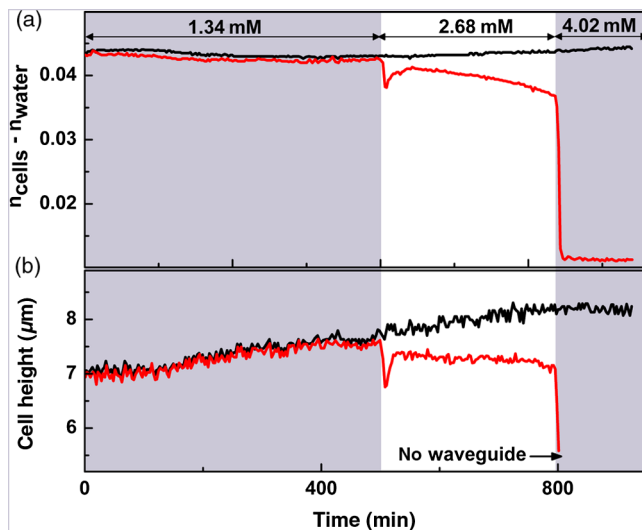


Fig. 5 Dynamics of IEC-18 cells refractive index n_{cell} (a) and average cell height (b) under prolonged exposure to different concentrations of EDTA. Red line corresponds to the chamber with low Ca^{2+} (treatment) and black line corresponds to the chamber with normal concentration of Ca^{2+} (control). Duration of the first stage (1.34 mM of EDTA) is 500 min. Duration of the second stage (2.68 mM of EDTA) is 300 min. Duration of the third stage (4.02 mM of EDTA) is 100 min. The temporal resolution of these measurements is 3 min.

cell–cell junctions have been injured). After the treatment, the cell height recovers, but it is still lower than that in the control chamber even after 20 h.

In the second experiment, we studied the effect of long-time exposure (500 and 300 min) of the cell monolayer to the growth medium supplemented with different concentrations of EDTA (Fig. 5). At the first step, we exposed the cell monolayer to the bathing medium containing 1.34 mM of EDTA for ~ 500 min. Figure 5 shows that the refractive index of the cells hardly changes under this treatment. We conclude that a minor decrease in extracellular Ca^{2+} concentration induced by this concentration of EDTA hardly affected the adherence and tight junctions and thus the integrity of the cell monolayer was kept intact. At the next stage, we replaced the growth medium with that containing a higher concentration of EDTA (2.68 mM) for ~ 300 min. This step caused a slow persistent decrease in the refractive index of the cells. We associate this with the fact that the decrease of extracellular Ca^{2+} concentration induced by enhanced concentration of EDTA slowly breaks cellular junctions and consequently decreases the height of the circumferential ring of actin filaments. At the beginning of this stage, a sharp drop in the cell refractive index was observed, which relaxed after ~ 50 min. This rapid change in the refractive index resulted most likely from the mechanical stress induced by the replacement of the growth medium. Notably, there was no change in the cell refractive index in the control chamber, though the medium in this chamber was similarly withdrawn and inserted back in order to simulate equal conditions in both chambers. Although exposure of the cells to the medium with the reduced concentration of Ca^{2+} at the first stage of the experiment did not disassemble adherence and tight junctions, it weakened the cell–cell attachment, thus even a minor mechanical stress initiated monolayer integrity breakdown. Finally, when we increased the concentration of EDTA to 4.02 mM,

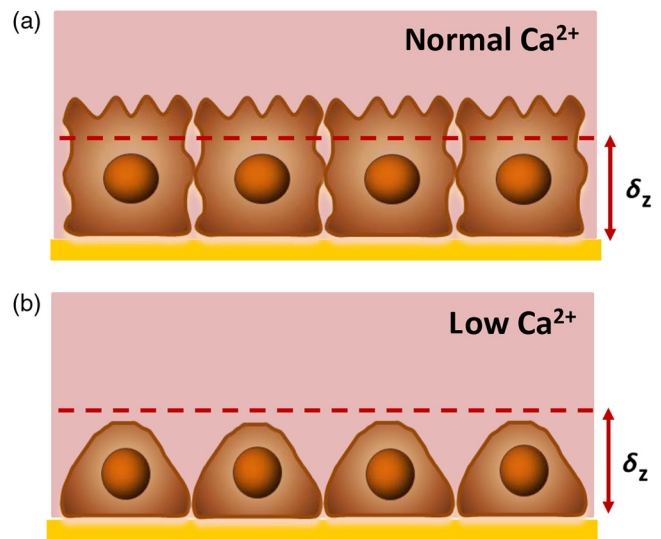


Fig. 6 Schematic model for the cell monolayer response to Ca^{2+} depletion. δ_z indicates the SP sampling height. (a) In the presence of normal Ca^{2+} concentration (1.8 mM), the cells form an intact monolayer and maintain healthy intercellular cell–cell junctions. (b) Under low Ca^{2+} conditions, cell–cell junctions are progressively damaged, leading to penetration of growth medium with the low refractive index into intercellular space. This results in the decrease in the cell monolayer refractive index as sampled by the SP wave. The average cell height under Ca^{2+} depletion drops.

the refractive index of the cell monolayer dropped dramatically. We associate this with a fast breakdown of adherence and tight junctions and loss of integrity of the cell monolayer.

The dynamics of the average cell height, as probed by the waveguide resonance [Fig. 5(b)], is consistent with this scenario. The cell layer can withstand small and intermediate Ca^{2+} depletion, but breaks down under severe Ca^{2+} depletion.

Figure 6 schematically summarizes the changes in cell monolayer morphology under Ca^{2+} depletion. At normal Ca^{2+} concentration, the cells form an intact monolayer and maintain healthy intercellular cell–cell junctions. Under low Ca^{2+} conditions, the cell–cell junctions are damaged, which leads to penetration of the growth medium into intercellular space. This process reduces the fraction of organic content f [Eq. (3)] inside the layer sampled by the SP wave, resulting in a decrease in the cells' monolayer refractive index.

5 Conclusions

We present here a label-free double-chamber SPR-based infrared biosensor for living cell studies. Since biological samples, and especially cell layers, are extremely complicated entities, there are plenty of normal, physiological reasons for differences between refractive indices of two different samples. The novelty of our biosensor is in the use of one homogeneous biological sample which is divided into two halves, where one half is exposed to treatment and the second half is simultaneously exposed to control media. By measuring the differences of the refractive indices of the two halves of the sample, we can extract the net influence of the stimulus and exclude all other causes for refractive index changes. Another advantage of the double-chamber biosensor is related to the fact that experiments utilizing cell layers are often run for hours and days, during which the cell layer naturally evolves. This evolution introduces uncertainty in a conventional one-chamber setup where the refractive index at the beginning of the measurement is taken as a reference. The problems associated with this uncertainty are easily solved with the continuous reference control measurement of the double-chamber biosensor. In this work, we used Ca^{2+} depletion procedures as a test case for the proof of concept. By running these basic biological experiments, we were able to show the strength of the double-chamber biosensor to provide accurate noise-free data about cellular dynamics.

We conclude that our FTIR-SPR double-chamber biosensor can eliminate major known artifacts from biological experiments that utilize cellular models. It allows unambiguous interpretation of the measurements and yields a 10-fold increase in the sensitivity compared to the single-chamber biosensor. We believe that our double-chamber biosensor will provide a new tool for continuous monitoring of fine dynamics of cell–cell and cell–substrate attachment, with the ability to track subtle changes induced by various treatments.

Acknowledgments

We are grateful to Professor Ronen Rapaport, Professor Nathalie Q. Balabanand, and Dr. Adi Vaknin for their professional advices and generous help in sharing their laboratory facilities. We acknowledge partial financial support from Yissum Research and Development Company of the Hebrew University of Jerusalem.

References

1. R. A. Blake, "Cellular screening assays using fluorescence microscopy," *Curr. Opin. Pharmacol.* **1**(5), 533–539 (2001).
2. M. A. Cooper, "Non-optical screening platforms: the next wave in label-free screening?," *Drug Discovery Today* **11**(23–24), 1068–1074 (2006).
3. M. A. Cooper, "Optical biosensors in drug discovery," *Nat. Rev. Drug Discovery* **1**(7), 515–528 (2002).
4. R. J. Leatherbarrow and P. R. Edwards, "Analysis of molecular recognition using optical biosensors," *Curr. Opin. Chem. Biol.* **3**(5), 544–547 (1999).
5. W. Lukosz and K. Tiefenthaler, "Sensitivity of integrated optical grating and prism couplers as (bio)chemical sensors," *Sens. Actuators* **15**(3), 273–284 (1988).
6. J. Homola, S. S. Yee, and G. Gauglitz, "Surface plasmon resonance sensors: review," *Sens. Actuators B* **54**(1–2), 3–15 (1999).
7. Y. Fang, "Non-invasive optical biosensor for probing cell signaling," *Sensors* **7**(10), 2316–2329 (2007).
8. M. Golosovsky et al., "Midinfrared surface-plasmon resonance: a novel biophysical tool for studying living cells," *J. Appl. Phys.* **105**(10), 102036 (2009).
9. J. J. Ramsden and R. Horvath, "Optical biosensors for cell adhesion," *J. Recept. Signal Transduction* **29**(3–4), 211–223 (2009).
10. V. Yashunsky et al., "Real-time monitoring of epithelial cell–cell and cell–substrate interactions by infrared surface plasmon spectroscopy," *Biophys. J.* **99**(12), 4028–4036 (2010).
11. R. Horvath et al., "Multidepth screening of living cells using optical waveguides," *Biosens. Bioelectron.* **24**(4), 799–804 (2008).
12. V. Yashunsky et al., "Surface plasmon-based infrared spectroscopy for cell biosensing," *J. Biomed. Opt.* **17**(8), 081409 (2012).
13. J. Voros et al., "Feasibility study of an online toxicological sensor based on the optical waveguide technique," *Biosens. Bioelectron.* **15**(9–10), 423–429 (2000).
14. R. T. Yamaguchi et al., "Real-time monitoring of cell death by surface infrared spectroscopy," *Appl. Phys. Lett.* **91**(20), 203902 (2007).
15. N. Zaytseva et al., "Microfluidic resonant waveguide grating biosensor system for whole cell sensing," *Appl. Phys. Lett.* **98**(16), 163703 (2011).
16. A. M. Castillo et al., "Myosin II actin interaction in MDCK cells: role in cell shape changes in response to Ca^{2+} variations," *J. Muscle Res. Cell Motil.* **19**(5), 557–574 (1998).
17. R. G. Contreras et al., "Interaction of calcium with plasma membrane of epithelial (MDCK) cells during junction formation," *Am. J. Physiol.* **263**(2 Pt 1), C313–C318 (1992).
18. L. Gonzalez-Mariscal et al., "Role of calcium in tight junction formation between epithelial cells," *Am. J. Physiol.* **259**(6 Pt 1), C978–C986 (1990).
19. H. Raether, "Surface plasmons on smooth and rough surfaces and on gratings," Chapter 2 in *Springer Tracks in Modern Physics*, G. Hohler, Ed., Vol. 111, Springer-Verlag, Berlin/New York (1988).
20. V. Lirtsman, M. Golosovsky, and D. Davidov, "Infrared surface plasmon resonance technique for biological studies," *J. Appl. Phys.* **103**(1), 014702 (2008).
21. C. L. Curl et al., "Refractive index measurement in viable cells using quantitative phase-amplitude microscopy and confocal microscopy," *Cytometry Part A* **65A**(1), 88–92 (2005).
22. F. P. Bolin et al., "Refractive-index of some mammalian-tissues using a fiber optic cladding method," *Appl. Opt.* **28**(12), 2297–2303 (1989).
23. A. Zilbershtein et al., "Quantitative surface plasmon spectroscopy: determination of the infrared optical constants of living cells," *Vib. Spectrosc.* **61**, 43–49 (2012).
24. Y. Fang et al., "Resonant waveguide grating biosensor for living cell sensing," *Biophys. J.* **91**(5), 1925–1940 (2006).
25. V. Yashunsky et al., "Real-time sensing of cell morphology by infrared waveguide spectroscopy," *PLoS One* **7**(10), e48454 (2012).
26. J. E. Bertie and Z. D. Lan, "Infrared intensities of liquids. 20. The intensity of the OH stretching band of liquid water revisited, and the best current values of the optical constants of $\text{H}_2\text{O}(l)$ at 25 degrees C between 15,000 and 1 cm^{-1} ," *Appl. Spectrosc.* **50**(8), 1047–1057 (1996).
27. M. Buskuhl and E. H. Korte, "Infrared-optical properties of vapour-deposited metal films," *Anal. Bioanal. Chem.* **374**(4), 672–675 (2002).

28. A. D. Rakic et al., “Optical properties of metallic films for vertical-cavity optoelectronic devices,” *Appl. Opt.* **37**(22), 5271–5283 (1998).
29. R. A. Desai et al., “Cell polarity triggered by cell–cell adhesion via E-cadherin,” *J. Cell Sci.* **122**(7), 905–911 (2009).
30. J. A. Scott et al., “Ena/VASP proteins can regulate distinct modes of actin organization at cadherin-adhesive contacts,” *Mol. Biol. Cell* **17**(3), 1085–1095 (2005).
31. M. Cerejido et al., “The making of a tight junction,” *J. Cell Sci. Suppl.* **17**, 127–132 (1993).
32. M. Cerejido, R. G. Contreras, and L. Gonzalez-Mariscal, “Development and alteration of polarity,” *Annu. Rev. Physiol.* **51**, 785–795 (1989).
33. E. Rodriguez-Boulan and W. J. Nelson, “Morphogenesis of the polarized epithelial cell phenotype,” *Science* **245**(4919), 718–725 (1989).
34. W. J. Nelson, D. J. Dickinson, and W. I. Weis, “Roles of cadherins and catenins in cell–cell adhesion and epithelial cell polarity,” *Prog. Mol. Biol. Transl. Sci.* **116**, 3–23 (2013).
35. C. T. Capaldo and I. G. Macara, “Depletion of E-cadherin disrupts establishment but not maintenance of cell junctions in Madin-Darby canine kidney epithelial cells,” *Mol. Biol. Cell* **18**(1), 189–200 (2006).
36. M. Cerejido, A. Ponce, and L. Gonzalezmariscal, “Tight junctions and apical basolateral polarity,” *J. Membr. Biol.* **110**(1), 1–9 (1989).
37. T. Fujimoto and K. Ogawa, “Energy-dependent transformation of mouse gallbladder epithelial-cells in a Ca-2+-depleted medium,” *J. Ultrastruct. Res.* **79**(3), 327–340 (1982).

Alexander Zilbershtein received a MA degree in physics from the Hebrew University of Jerusalem in 2007. Currently, he is a PhD student in Rakah Institute of Physics, The Hebrew University of Jerusalem. His research interests are focused on spectroscopy based on infrared surface plasmon and its utilization for living cells biosensing. He is working in collaboration with biologists on the development of a novel FTIR-SPR biosensor for the study of living cells.

Amir Bein received a BSc degree in nutritional sciences from the Hebrew University of Jerusalem in 2008. He is conducting his research, at the Hebrew University of Jerusalem, toward his PhD

degree. He worked in collaboration with physicists on the development of a novel FTIR-SPR biosensor for the study of living cells. His interests are cellular mechanisms involved in the disruption of the intestinal barrier, cellular junction structures and dynamics, and real time and label-free biosensing.

Vladislav Lirtsman received a PhD degree in physics from the Hebrew University of Jerusalem in 2008. From 2008 to 2011, he was a postdoctoral fellow at the Hebrew University. He began his career as a researcher of crystals strength and plasticity and X-ray crystals structure at the Institute for Low Temperature Physics and Engineering, Academy of Science of Ukraine in 1990. In the last years, he worked on project of implementation of infrared surface plasmon method to live cells studies.

Betty Schwartz received a PhD degree from Ben-Gurion University, Beer-Sheva, Israel. From 1990 to 1993, she was a postdoctoral fellow at the University of San-Francisco, California. From 1996 onward, she is appointed as an associate professor at the Institute of Biochemistry, Food Science and Nutrition at the Hebrew University of Jerusalem, Israel. From 2005 to 2011, she served as a head of the School of Nutritional Sciences. Her research interests are focused on the anticarcinogenic and anti-inflammatory effects of nutrients.

Michael Golosovsky is a researcher in the Racah Institute of Physics. His research interests are in experimental solid state physics, magnetic resonance, microwave and infrared spectroscopy. Recently, he has been developing label-free biosensors, based on surface plasmon resonance, and their application for live cell studies.

Dan Davidov is a professor emeritus at the Racah Institute of Physics of the Hebrew University of Jerusalem. He is holding the Louis and Ida Shlansky chair of physics. He has long interests in condensed matter physics including magnetism, superconductivity, magnetic resonance, polymers, and biopolymers. His recent research is related to infrared surface plasmon propagating in live cells. His group published many papers on the effect of drugs and bacteria on live cells.